Politecnico di Torino

Master degree course in Physics of complex systems

Master degree thesis

Thermalization of photons in disordered scattering media

Supervisors
Valentina Krachmalnicoff
Romain Pierrat
Luca Fausto Tocchio

Candidate
Lorenzo Soncin

Academic Year 2023-2024

Abstract

Photons represent the most common Bose gas. The sun or thermal light sources are examples of black body radiators that we encounter every day. Unlike other Bose gases, photons exhibit a vanishing chemical potential, meaning that their number is not conserved when the temperature of the black body is varied. This results in the impossibility of obtaining a Bose-Einstein Condensate (BEC) of light, because as the temperature decreases, the photons simply fade. However, in 2010, a BEC of photons was first realized in the group of M. Weitz at the University of Bonn. This was achieved inside an optical microcavity after a process that ensures the photons follow the Bose-Einstein distribution with a non-zero chemical potential, i.e., thermalization. In this work, I will present how I have been attempting to reproduce such a thermalization process, where light is trapped not by a microcavity, but by a disordered scattering medium. This will be done first by introducing the theoretical foundations of the thermalization process and a simple diffusion model to treat the scatterers. Then the results of the experiments will be presented and finally they will be supported by a more refined model that was numerically solved on a cluster of processors.

Contents

Chapter 1

Introduction

By the late XIX century, significant theoretical advancements spearheaded by prominent figures such as Kirchhoff, Wien, Rayleigh, Jeans and Planck [3] concentrated on characterizing the thermal spectrum of a black body, specifically its emission and absorption properties when in equilibrium with a thermal bath at temperature T.
The correct solution for the black body problem was found by Planck in a series of milestone papers [14] [15] [16] [17] [18], where he first introduced the quantization of energy, leading to the celebrated Planck's law for the spectral density of radiation of a black body given by

$$u(\omega, \beta) = \frac{\hbar\omega^3}{\pi^2 c^3} \frac{1}{e^{\beta\hbar\omega} - 1}, \tag{1.1}$$

where $\beta = 1/(k_B T)$.
Nowadays, the very same results can be obtained by taking into account the bosonic nature of photons. It follows that the number density of particles in the grand canonical description of a photon gas must follow the Bose-Einstein distribution

$$n_{ph} = \frac{1}{e^{\beta(\hbar\omega - \mu)} - 1}, \tag{1.2}$$

where μ is the chemical potential. Therefore, Eq. (1.1) is straightforward, since [3]

$$u(\omega, \beta) \propto \omega^3 n_{ph} \tag{1.3}$$

and if $\mu = 0$ one recovers Eq. (1.1).
The vanishing chemical potential of a black body infers that the temperature controls n_{ph} and therefore when T decreases n_{ph} vanishes. This implies that a macroscopic population of the ground state is not feasible in such a situation. This has long prevented the realization of a Bose-Einstein Condensate (BEC) of photons. A non vanishing chemical potential could allow to overcome this problem since when $\mu \neq 0$ it is possible to experimentally control the number of photons even at low temperatures.

In 2010, Klaers et al. experimentally realized a BEC of photons [7]. However, before moving towards a BEC, it is necessary to obtain a gas of photons with a non-vanishing chemical potential. This is achieved by a thermalization process that consists of many cycles of absorption and emission of the photons by fluorescent molecules that act all together as the chemical reservoir of the Grand Canonical Ensemble (GCE). A fundamental requirement for obtaining many cycles of absorption and emission is to maintain the interaction between the photons and the molecules for a sufficient amount of time. This was accomplished in [7] by trapping the light inside an optical

micro-cavity.
My internship project is placed in this framework. Taking inspiration from the random laser [2], I have been working on the theoretical, numerical, and experimental aspects to obtain a thermalization process in a system where the light is trapped inside a dye solution (Rhodamine 6G in water solution), not by a micro-cavity but by a disordered scattering medium (Polystyrene micro particles) that mimics the effect of a cavity.
In the following pages, I will present a theoretical model to describe the thermalization process and introduce a simple diffusive model to treat the scatterers (chapter 2), describe the experimental setup and the obtained results (chapter 3), introduce a more refined model to treat the light propagation in a scattering medium and present its numerical implementation on a cluster of processors with the consequent numerical results (chapter 4).

Chapter 2

Theoretical model for thermalization

The system under analysis is a gas of photons in a disordered scattering medium that is exchanging particles with fluorescent molecules (chemical reservoir). Both the gas of photons and the molecules will be modelled as in [6] and [20]. Here I will show that if

1. The Kennard Stepanov law is satisfied
2. Chemical equilibrium between photons, excited, and ground-state molecules is achieved

then the system is at thermal equilibrium and by balancing the absorption and emission rates Eq. (1.2) is recovered. The scattering dynamics will be treated first in this chapter with a simple diffusive model and then with a more refined radiative transfer one (see chapter 4).

2.1 Molecular model and Kennard-Stepanov law

In this section, I derive the Kennard-Stepanov law which is an important result to understand photon thermalization. A fluorescent molecule can be modeled as a 2 level system as in Fig. 2.1. Let α (respectively σ) represent the sets of rotovibrational sublevels of the electronic ground state $|0\rangle$ (respectively excited state $|1\rangle$) . Let ω be the frequency of the absorbed or stimulated emitted photon during an electronic transition between sublevels $|\alpha\rangle$ and $|\sigma\rangle$. The Einstein coefficients represent the transition rates from one level to the other. They can be expressed as averages over all possible rotovibronic transitions and they are given by

$$B_{01}(\omega) = \sum_{\alpha,\sigma} p_\alpha B_{\alpha\sigma}(\omega) \tag{2.1}$$

(transition rate from $|0\rangle$ to $|1\rangle$) and

$$B_{10}(\omega) = \sum_{\alpha,\sigma} p_\sigma B_{\sigma\alpha}(\omega) \tag{2.2}$$

(transition rate from $|1\rangle$ to $|0\rangle$).
Here, p_α (respectively p_σ) denotes the probability that the molecule is in state α (respectively σ), and $B_{\alpha\sigma}$ and $B_{\sigma\alpha}$ are the Einstein coefficients for rotovibronic transitions between individual rotovibrational states belonging to different electronic levels.
The time required for the molecules to thermalize through collisions with the solvent molecules is

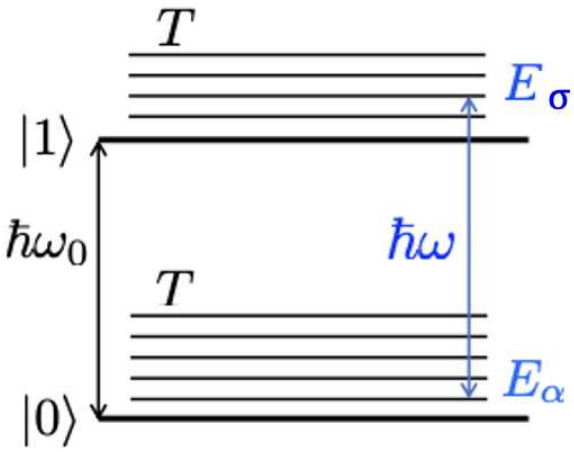

Figure 2.1: The Jablonski diagram depicts the molecular energy levels interacting with light. The ground and excited electronic states, $|0\rangle$ and $|1\rangle$, are separated by an energy gap of approximately $\hbar\omega_0$. The thin lines illustrate the rotovibrational sublevels within each electronic state.

much shorter than all the time scales involved in the optical dynamics. This is why fluorescence can be dissipative (Stokes shift), and there typically is no correlation between the wavelength of the absorbed and emitted photon (Kasha's rule). Consequently, the molecules can be considered to be in thermal equilibrium with the solvent. This means that a generic energy level $|\alpha\rangle$ follows the Boltzmann distribution (the molecules form a canonical ensemble)

$$p_\alpha = \frac{\exp\left(-\beta E_\alpha\right)}{Z_0} \tag{2.3}$$

where Z_0 is the partition function

$$Z_0 = \sum_\alpha \exp\left(-\beta E_\alpha\right) = \int_0^\infty g(E)\exp\left(-\beta E\right) dE \tag{2.4}$$

and $g(E)$ is the density of states defined by

$$g(E) = \sum_\alpha \delta(E - E_\alpha) \tag{2.5}$$

and equivalently for the sublevel $|\sigma\rangle$ ($Z_0 \to Z_1$).
Conservation of energy $E_\alpha + \hbar\omega = E_\sigma + \hbar\omega_0$ implies that

$$p_\sigma = p_\alpha \frac{Z_0}{Z_1} \exp\left(-\beta\hbar(\omega - \omega_0)\right). \tag{2.6}$$

Exploiting this last relation and the symmetry of the problem ($B_{\alpha\sigma} = B_{\sigma\alpha}$), the ratio between the two Einstein coefficients leads to [4] [5] [11] [19] [21]

$$\frac{B_{10}(\omega)}{B_{01}(\omega)} = \frac{Z_0}{Z_1}\exp(-\beta\hbar(\omega - \omega_0)). \tag{2.7}$$

Experimentally, it is possible to measure the absorption $\sigma_a(\omega) \propto B_{01}(\omega)$ and the emission cross section $\sigma_{em}(\omega) \propto B_{10}(\omega)$. Therefore, Eq. (2.7) can be recast as

$$\frac{\sigma_{em}(\omega)}{\sigma_a(\omega)} = \frac{Z_0}{Z_1} \exp\left(\frac{-\hbar(\omega - \omega_0)}{k_B T}\right) \tag{2.8}$$

This is the Kennard-Stepanov law.

2.2 Chemical equilibrium

As for the photons, it is necessary to use a grand canonical description for both the molecules in the ground state and those in the excited state since their number is allowed to vary. The probabilities of finding a molecule in the ground or the excited states are given by

$$p_0 = \frac{\rho_0}{\rho} = \frac{Z_0 e^{\beta\mu_0}}{\Xi} \tag{2.9}$$

$$p_1 = \frac{\rho_1}{\rho} = \frac{Z_1 e^{-\beta(\hbar\omega_0 - \mu_1)}}{\Xi} \tag{2.10}$$

where ρ_0 is the density of the ground state molecules and ρ_1 is the density of the excited ones. Trivially, $\rho = \rho_1 + \rho_0$. Ξ is the grand partition function. The process described in Eq. (2.1) is a photo-chemical reaction of the type

$$\gamma + |\alpha\rangle \rightleftharpoons |\sigma\rangle \tag{2.11}$$

where γ stands for the photon, $|\alpha\rangle$ stands for molecule in one of the rotovibronic sublevels of the ground state and $|\sigma\rangle$ for a rotovibronic sublevel of the excited state. In chemical equilibrium, the chemical potential of the different species are linked by

$$\mu_\gamma + \mu_0 = \mu_1 \tag{2.12}$$

that can be expressed in terms of the fugacity

$$z = e^{\beta\mu_\gamma} = \frac{e^{\beta\mu_1}}{e^{\beta\mu_0}}. \tag{2.13}$$

Combining Eq. (2.13) with Eq. (2.9) and Eq. (2.10), it is possible to get

$$z = e^{\beta\mu_\gamma} = \frac{Z_0\rho_1}{Z_1\rho_0} e^{\beta\hbar\omega_0}. \tag{2.14}$$

This shows that the chemical potential of the photons is fixed by the ratio ρ_1/ρ_0. This is weakly affected by the absorption and emission of the photons and is then fixed by the external pumping because the number of molecules largely exceeds the number of photons inside the system.

2.3 Thermalization process

The time evolution of a physical system coupled with a bath can be seen as a Markov chain [9] [12]. Here, I will show how the photons thermalize with the molecules' chemical reservoir through many absorption and emission events.
Let us call $|K\rangle = |n_{\mathbf{k}_1 T_1}, n_{\mathbf{k}_2 T_2}, n_{\mathbf{k}_3 T_3}, ..., n_{\mathbf{k}_i T_i}, ...\rangle$ a state of the electromagnetic field in the Fock space. This means that for each mode i there are $n_{\mathbf{k}_i T_i}$ photons with wave vector $\mathbf{k}_i$, polarization T_i = 1,2, and pulsation $\omega(\mathbf{k_i}) = c|\mathbf{k}_i|$ (let's suppose that the field is confined in a box of volume

$V = L_x L_y L_z$ and then make the length of the box L_j go to infinity to consider all the space). To have a complete description of the system and take into account also the molecules, one could think about an enlarged state $|KM\rangle = |n_{\mathbf{k}_1 T_1}, n_{\mathbf{k}_2 T_2}, n_{\mathbf{k}_3 T_3}, ..., n_{\mathbf{k}_i T_i}, ...\rangle \otimes |\psi\rangle$ but let's focus just on the gas of photons.
The temporal evolution of the probability for the field to be in state $|K\rangle$ at time t follows the master equation

$$p_K(t+1) = \sum_{K'} p_{K'}(t) R(K' \to K), \tag{2.15}$$

where $\mathbf{R}$ is the stochastic matrix and its elements $R(K' \to K) = P(K|K')$ represent the probability to jump from state K' to state K. Because of normalization $\mathbf{R}$ satisfies the following constrain

$$\sum_{K} R(K' \to K) = 1 \tag{2.16}$$

that allows to rewrite Eq. (2.16) as

$$p_K(t+1) - p_K(t) = \sum_{K' \neq K} \left[p_{K'}(t) R(K' \to K) - p_K(t) R(K \to K') \right], \tag{2.17}$$

Requiring thermal equilibrium for long times means that $P_K(t)$ must approach the grand canonical probability distribution as t increases, i.e.,

$$p_K(t \to \infty) = \frac{\exp(-\beta(E_K - \mu_\gamma N_K))}{\Xi} \tag{2.18}$$

where E_K is the energy of state $|K\rangle$ and N_K is the total number of photons in state $|K\rangle$. It is necessary then to solve the steady state master equation (right hand side of Eq. (2.17) equal to 0) to obtain the constrain under which stocastic matrix must lie. This has many solutions but the detailed balance condition can be taken as a probabilistic definition of thermal equilibrium

$$\frac{R(K \to K')}{R(K' \to K)} = \frac{p_{K'}(t \to \infty)}{p_K(t \to \infty)} = \exp\left[-\beta(\Delta E - \mu_\gamma \Delta N)\right] \quad \forall K, K' \tag{2.19}$$

where $\Delta E = E_{K'} - E_K$ and $\Delta N = N_{K'} - N_K$. In first order perturbation theory the rate of transition (per volume) for the absorption of a photon in mode i at position $\mathbf{r}$ is given by [6]

$$R_{01}^{K,i}(\mathbf{r}) = B_{01}(\omega) u_i(\mathbf{r}) \rho_0 n_{\mathbf{k}_i T_i} \tag{2.20}$$

where $u_i(\mathbf{r})$ is the spectral energy density of one photon in mode i. Equivalently for the emission process, the matrix element is given by

$$R_{10}^{K,i}(\mathbf{r}) = B_{10}(\omega) u_i(\mathbf{r}) \rho_1 (n_{\mathbf{k}_i T_i} + 1) \tag{2.21}$$

Let us consider the absorption process where the state of the system changes from $|K\rangle \to |K'\rangle$ by the absorption of one photon in mode i. Then after the event $n'_{\mathbf{k}_i T_i} = n_{\mathbf{k}_i T_i} - 1$. Conversely, state $|K\rangle$ is generated by the emission of a photon from state $|K'\rangle$ in mode i. Because of def. (2.19), the Markov process described by transition rates Eq. (2.20) and Eq. (2.21) is at thermal equilibrium if

$$\frac{R_{01}^{K,i}(\mathbf{r})}{R_{10}^{K,i}(\mathbf{r})} = \exp\left[\beta(\hbar\omega_i - \mu_\gamma)\right]. \tag{2.22}$$

Indeed, in an absorption event of a photon with pulsation $\omega_i = c|\mathbf{k_i}|$, the energy variation is $\Delta E = -\hbar\omega_i$ and $\Delta N = -1$. For such a process, the ratio of the rates leads to

$$\frac{R_{01}^{K,i}(\mathbf{r})}{R_{10}^{K,i}(\mathbf{r})} = \frac{B_{01}(\omega_i)\rho_0}{B_{10}(\omega_i)\rho_1}. \tag{2.23}$$

If the Kennard-Stepanov law (Eq. (2.7)) is satisfied and chemical equilibrium Eq. (2.14) is met, then Eq. (2.22) is fulfilled and after many cycles of absorption and emission, thermal equilibrium is reached ($t \to +\infty$, to be clarified in Sec. 2.4). Indeed plugging Eq. (2.7) into Eq. (2.23) one gets

$$\frac{R_{01}^{K,i}(\mathbf{r})}{R_{10}^{K,i}(\mathbf{r})} = \frac{\rho_0}{\rho_1}\frac{Z_1}{Z_0}\exp\left[\beta\hbar(\omega_i - \omega_0)\right]. \tag{2.24}$$

Now inverting Eq. (2.14) to obtain the ratio ρ_0/ρ_1 and putting it in the previous expression one gets

$$\frac{R_{01}^{K,i}(\mathbf{r})}{R_{10}^{K,i}(\mathbf{r})} = \frac{Z_0}{Z_1}\exp\left[\beta(\hbar\omega_0 - \mu_\gamma)\right]\frac{Z_1}{Z_0}\exp\left[\beta\hbar(\omega_i - \omega_0)\right] = \exp\left[\beta(\hbar\omega_i - \mu_\gamma)\right], \tag{2.25}$$

that is Eq. (2.22).
Now it is possible to recover the Bose-Einstein distribution $n_{\mathrm{ph}}(\omega)$ for the gas of photons with a non-zero chemical potential. Considering first a simple situation where the translational invariance holds, it si possible to assume that the number of photons per unit volume $n(\omega, t)$ does not depend on the position. This allows considering ρ_0 and ρ_1 as uniform in space. The number of photons per unit volume follows then

$$\frac{\partial n(\omega,t)}{\partial t} = -\rho_0\sigma_a(\omega)v_E n(\omega,t) + \rho_1\sigma_{\mathrm{em}}(\omega)v_E n(\omega,t) + \rho_1\sigma_{\mathrm{em}}(\omega)v_E\mathcal{N}(\omega) \tag{2.26}$$

where v_E is the velocity of light inside the system. This equation is obtained by considering all the mechanism that allow the number of photons to vary. Here,

- the first term on the right-hand side describes absorption,
- the second term on the right-hand side describes stimulated emission,
- the third term on the right-hand side describes spontaneous emission where $\mathcal{N}(\omega)$ is the density of states of the electromagnetic field,

$n(\omega, t)$ is linked to the average number density of photons per mode $n_{\mathrm{ph}}(\omega, t)$ by

$$n(\omega,t) = n_{\mathrm{ph}}(\omega,t)\mathcal{N}(\omega) \tag{2.27}$$

and this allows rewriting Eq. (2.26) as

$$\frac{\partial n_{\mathrm{ph}}(\omega,t)}{\partial t} = -\rho_0\sigma_a(\omega)v_E n_{\mathrm{ph}}(\omega,t) + \rho_1\sigma_{\mathrm{em}}(\omega)v_E[n_{\mathrm{ph}}(\omega,t)+1] \tag{2.28}$$

To deduce the shape of n_{ph} in the thermalized regime, it is necessary to impose again the Kennard-Stepanov law Eq. (2.7), chemical equilibrium Eq. (2.14), and stationarity, i.e., $\partial n_{\mathrm{ph}}(\omega,t)/\partial t = 0$ leading to the Bose-Einstein distribution

$$n_{\mathrm{ph}}(\omega) = \frac{1}{e^{\beta(\hbar\omega-\mu_\gamma)}-1} \tag{2.29}$$

as expected.

2.4 Simple diffusion model and time scales

As anticipated in the introduction, the photons must maintain interaction with the molecules for a sufficiently long time to reach the Bose-Einstein distribution. This is accomplished by dispersing the molecules in a scattering medium instead of placing them in a micro-cavity, as previously

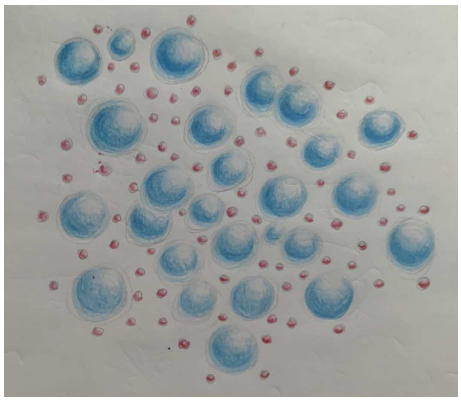

Figure 2.2: Pictorial representation of light scattering in a disordered medium: the blue spheres represent the scatterers and the red dots the rhodamine molecules.

done in Ref. [7].

With a similar approach to the one used in Ref. [10], it is possible to include the effects of the scatterers in Eq. (2.26). Let us consider ρ_0 and ρ_1 fixed and homogeneous. It is useful to introduce the transport mean free path ℓ_t that is related to the scattering mean free path ℓ_s by

$$\ell_t(\omega) = \frac{\ell_s(\omega)}{1 - g(\omega)}. \tag{2.30}$$

Here

- $\ell_s(\omega) = 1/(\rho_s \sigma_s(\omega))$ can be seen as the average length travelled by a photon between two scattering events. $\sigma_s(\omega)$ is the scattering cross section and ρ_s the number density of scatterers.
- $g(\omega)$ is called anisotropy factor and tells how anisotropic is the scattering process (for a single scatteriing event).

Given these two definitions, it is possible to give a interpretation of the transport mean free path: it is the average distance over which the diffused intensity becomes isotropic. If $g = 0$ then $\ell_t = \ell_s$. If $g \to 1$ then $\ell_t \to +\infty$ meaning that the diffused intensity will never be isotropic due to the presence of a strictly forward intensity at each scattering event. If the typical size scale of the system R is much greater than the photon transport mean free path ℓ_t, i.e., $R \gg \ell_t$, the number of photons per unit volume follows

$$\begin{aligned}\frac{\partial n(\mathbf{r},\omega,t)}{\partial t} = D\nabla^2 n(\mathbf{r},\omega,t) - \rho_0 \sigma_a(\omega) v_E n(\mathbf{r},\omega,t) + \rho_1 \sigma_{\text{em}}(\omega) v_E n(\mathbf{r},\omega,t) \\ + \rho_1 \sigma_{em}(\omega) v_E \mathcal{N}(\omega)\end{aligned} \tag{2.31}$$

where now

- $n(\mathbf{r},\omega,t)$ depends on the position because of the scattering medium,
- the Laplacian term describes the diffusion mechanism due to scattering with $D = v_E \ell_t/3$, the photon diffusion constant,
- the last 3 terms describe the absorption and emission mechanism as in Eq. (2.26).

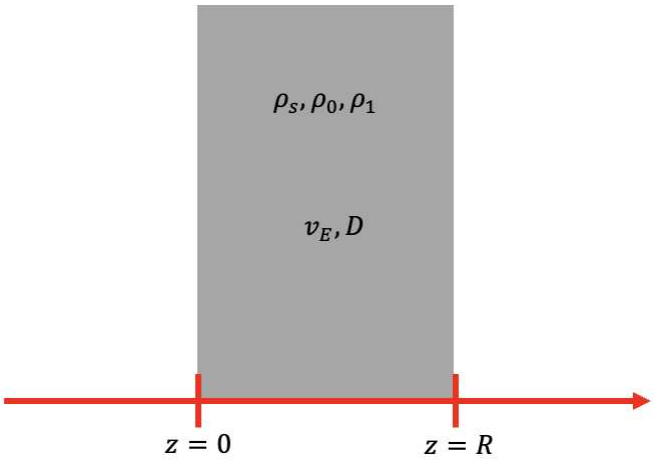

Figure 2.3: Representation of a slab geometry. The grey part represents the slab where is present a concentration of scatterers ρ_s, ρ_0 of ground state molecules and ρ_1 of excited molecules. It is characterized by a velocity of light v_E and a diffusion constant D.

Equation (2.31) is the result of the coupling of a diffusion equation with the rate equation Eq. (2.26). By merging into a single effective absorption cross-section the absorption and emission ones like

$$\rho\sigma_a'(\omega) = \rho_0\sigma_a - \rho_1\sigma_{\text{em}}, \tag{2.32}$$

Equation (2.31) becomes

$$\frac{\partial n(\mathbf{r},\omega,t)}{\partial t} = D\nabla^2 n(\mathbf{r},\omega,t) - \rho\sigma_a'(\omega)v_E n(\mathbf{r},\omega,t) + \rho_1\sigma_{\text{em}}(\omega)v_E\mathcal{N}(\omega). \tag{2.33}$$

This equation has an analytical solution if a slab geometry depicted in Fig. 2.3 is considered: invariant in x and y considering the molecules and the scattering medium being placed between $z_0 = 0$ and $z_1 = R$. Therefore $n(\mathbf{r},\omega,t) = n(z,\omega,t)$. This calls for the following Dirichlet problem

$$\begin{cases} n(0,\omega,t) = n(R,\omega,t) = 0 \\ n(z,\omega,0) = \delta(z) \end{cases} \tag{2.34}$$

This problem admits the following solution

$$\begin{aligned} n(z,\omega,t) = \frac{4}{\pi}\mathcal{N}(\omega)\sum_{k=0}^{+\infty} \frac{1}{\frac{\rho\sigma_a'(\omega)}{\rho_1\sigma_{\text{em}}(\omega)} + (2k+1)^2\frac{R^2}{D\pi^2\rho_1\sigma_{\text{em}}(\omega)}} \sin\left(\frac{\pi(2k+1)z}{R}\right) \\ \times \frac{1-\exp\left[-tv_E\sigma_a'(\omega) - (2k+1)^2 t\frac{\pi^2 D}{R^2}\right]}{2k+1}. \end{aligned} \tag{2.35}$$

This expression is a superposition of many different spatial modes defined by k. Even though this is the solution for a very simple and non-physical geometry (the slab has infinite dimension along x and y and it is uniformly pumped), it gives a first insight into the timescale involved in the problem. These are

1. $\tau_D = \frac{1}{\pi^2}\frac{R^2}{D}$ is the characteristic time that the light needs to diffuse in the system,

2. $\tau'_a(\omega) = \frac{1}{\rho\sigma'_a(\omega)v_e}$ it's the characteristic time of the effective absorption,

3. $\tau_{\rm em}(\omega) = \frac{1}{\rho_1\sigma_{\rm em}(\omega)v_E}$ it's the characteristic time of the spontaneous emission.

Equation (2.35) can be rewritten as

$$n(z,\omega,t) = \frac{4}{\pi}\mathcal{N}(\omega)\sum_{k=0}^{+\infty}\frac{1}{\frac{\tau_{\rm em}(\omega)}{\tau'_{\rm a}(\omega)} + (2k+1)^2\,\frac{\tau_{\rm em}(\omega)}{\tau_D}}\sin\left(\frac{\pi(2k+1)z}{R}\right) \times\frac{1-\exp\left[-\frac{t}{\tau'_{\rm a}} - (2k+1)^2\frac{t}{\tau_D}\right]}{2k+1}. \tag{2.36}$$

This solution converges if $\tau_D > 0$ and $\tau'_a > 0$. For sufficiently long times, the exponential vanishes and the density of photons will look like

$$n(z,\omega,t) = \frac{4}{\pi}\mathcal{N}(\omega)\sum_{k=0}^{+\infty}\frac{1}{\frac{\tau_{\rm em}(\omega)}{\tau'_{\rm a}(\omega)}\left[1+(2k+1)^2\,\frac{\tau'_{\rm a}(\omega)}{\tau_D}\right]}\frac{\sin\left(\frac{\pi(2k+1)z}{R}\right)}{2k+1} \tag{2.37}$$

Interestingly,

$$\frac{\tau_{\rm em}(\omega)}{\tau'_{\rm a}(\omega)} = \frac{\rho_0\sigma_a(\omega)}{\rho_1\sigma_{em}(\omega)} \propto e^{\beta(\hbar\omega-\mu_\gamma)} - 1 \tag{2.38}$$

under the hypotheses presented at the beginning of the chapter: validity of the Kennard-Stepanov law Eq. (2.7) and chemical equilibrium Eq. (2.14). The latter is expected to arise for $\tau'_a \ll t \ll \tau_D$. Therefore, at least for $k = 0$, if

$$\frac{\tau'_a(\omega)}{\tau_D} \ll 1 \tag{2.39}$$

the number of photons per unit volume is proportional to the Bose-Einstein distribution. Moreover, for as many k as the relation

$$\frac{\tau'_a(\omega)}{\tau_D} \ll (2k+1)^2 \tag{2.40}$$

is verified, then as many modes will exhibit Bose-Einstein behavior. Indeed if the latter holds Eq. (2.37) can be rewritten as

$$n(z,\omega,t) \approx \frac{4}{\pi}\mathcal{N}(\omega)\sum_{k=0}^{+\infty}\frac{1}{e^{\beta(\hbar\omega-\mu_\gamma)}-1}\frac{\sin\left(\frac{\pi(2k+1)z}{R}\right)}{2k+1}, \tag{2.41}$$

which is saying the the spectral distribution of density o photons follows the Bose-Einstein distribution.

This result, even if obtained with a very simple model, shows that the thermalized regime should be experimentally reachable. The purpose of the next chapter is to investigate it.

To catalog the different implementations of the experiment it is now possible to define different regimes where it makes sense to think about different types of timescales. The typical time spent by a photon inside the system is called τ_H, Thouless time, and it will be computed in different ways depending on the regime:

- $R \ll \ell_s$: Ballistic propagation, in this case $\tau_H = \tau_b = R/v_E$
- $R \sim \ell_s$: Single-scattering regime, no analytical time can be computed.
- $\ell_s \ll R \ll \ell_t$: Multiple-scattering regime, no analytical time can be computed.
- $\ell_t \ll R$: Diffusive regime where the diffusion equation is valid, then $\tau_H = \tau_D = R^2/(\pi^2 D)$

Chapter 3

Experimental setup and results

In this chapter, I will present the experimental setup used to conduct the measurements, the analyzed samples, and the obtained results.

3.1 Experimental setup

The experiments were performed with a super-continuum laser, which is a pulsed laser (pulse duration of the order of 100 ps) with a spectrum that covers all the visible and extends to the infrared. For our experiments, the laser was filtered either around 480 nm or 460 nm with a variable bandwidth that will be specified for each presented dataset. The setup was mounted on an optical breadboard.

As shown in Fig. 3.1, the laser light comes out from an optical fiber. It is then collimated using a lens with a focal length of 19 mm. The size of the collimated beam is controlled by a diaphragm. Two mirrors are used to adjust the position of the beam and direct it towards the sample.

The emitted photons are collected perpendicularly to the direction of the pump beam, through a lens placed in the $2f$ configuration, as shown in Fig. 3.1. They are collected by an optical fiber with a numerical aperture of 0.22 and sent to a spectrometer. An optical filter is placed in front of the collection fiber to remove stray laser light and collect only the photons emitted by the fluorophores that were scattered by the sample.

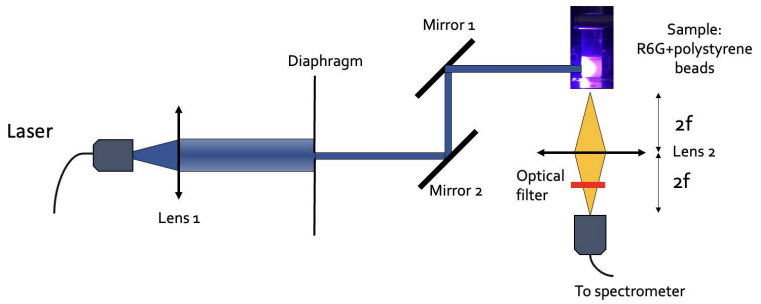

Figure 3.1: Scheme of the experimental setup

3.2 Absorption and emission cross section

The frequency range where the Bose-Einstein distribution is expected to arise is the one where the Kennard-Stepanov law reported in Eq. (2.7) is satisfied. By taking the logarithm of Eq. (2.7) one obtains

$$\ln \frac{\sigma_{em}(\omega)}{\sigma_a(\omega)} = \ln \frac{Z_0}{Z_1} - \beta\hbar(\omega - \omega_0). \tag{3.1}$$

Therefore the aforementioned region is the one where the logarithm of the ratio of the absorption and emission cross sections has a linear behavior.

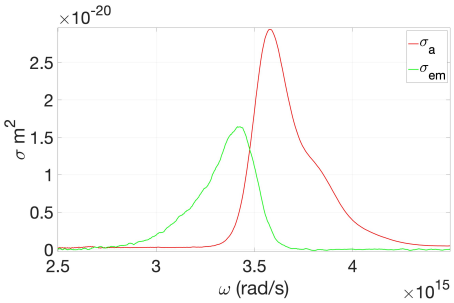

(a) This graph shows the absorption (σ_a) and the emission (σ_{em}) cross sections of the fluorophore rhodamine 6G. These have been measured thanks to a spectrometer available at Institut Langevin.

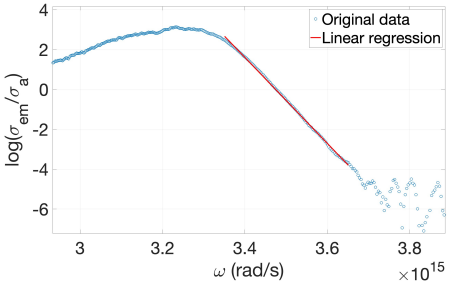

(b) This graph shows $\ln(\sigma_{em}(\omega)/\sigma_a(\omega))$ (dotted curve) as a function of ω. The solid red line represents a linear interpolation of the experimental data where the Kennard-Stepanov law is satisfied.

Figure 3.2: Absorption and emission properties

Fig. 3.2a shows the absorption and emission cross sections superimposed on the same graph. From Fig. 3.2b it is clear that the range of frequencies where Eq. (2.7) is satisfied goes from $3.35 \cdot 10^{15}$ rad/s to $3.65 \cdot 10^{15}$ rad/s that is from 516 nm to 562 nm. Therefore, this is the interval where the Bose-Einstein distribution is expected to appear. From the slope m obtained from the linear fit presented in Fig. 3.2b, it is possible to define an effective temperature

$$T_{\text{eff}} = -\frac{\hbar}{k_B m} = 355\,\text{K}. \tag{3.2}$$

The effective temperature found with this method is way larger than room temperature (293 K) which is the temperature at which the data were acquired. This discrepancy between the temperature of the reservoir and the temperature deduced from the spectrum has already been reported in the literature [8] as an effect of spectral broadening or a non-thermalization of the rotovibrational levels. One can then define a new temperature which is called spectral temperature as follows [8]:

$$T_{\text{spec}}(\omega) = -\frac{\hbar}{k_B \frac{d\ln}{d\omega}\frac{\sigma_{em}(\omega)}{\sigma_a(\omega)}}. \tag{3.3}$$

Figure 3.3a and 3.3b show respectively a comparison between the spectral temperature obtained from the emission and absorption cross sections that I have measured, and the one that can be found in [8]. Except for some aberrations at the lowest wavelengths, these two datasets are in good agreement. I will therefore consider $T \approx T_{\text{spec}}(\omega)$ in the frequency/wavelength range under analysis.

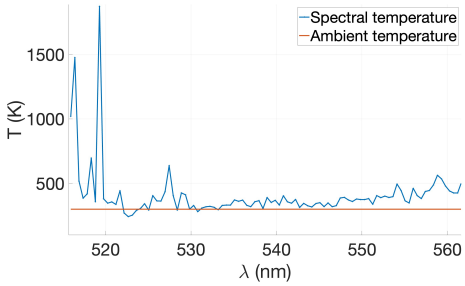

(a) Spectral temperature $T_{spec}(\lambda)$ obtained from the experimental data reported in Figure 3.2a as a function of the wavelength λ.

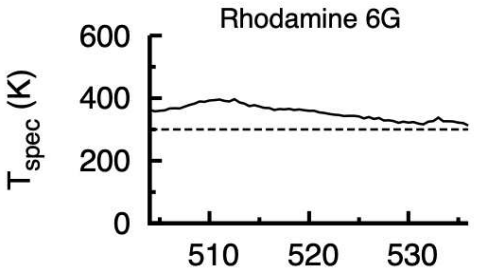

(b) Spectral temperature $T_{spec}(\lambda)$ as reported in [8]

Figure 3.3: Spectral Temperature

3.3 Samples' description

The samples under study were water solutions of rhodamine 6G (R6G) filled with polystyrene micro-beads of 200 nm in diameter. The solutions were contained inside a cylindrical flask of diameter 1.5 cm and height 7cm. Different concentrations of both R6G and beads were used. To differentiate the samples and present the results, the following notation will be used:

$$P\%R\% \tag{3.4}$$

where $R\%$ stands for the percentage of rhodamine (fluorophore) concentration calculated with respect to a reference one and the same for the $P\%$ percentage of polystyrene beads (scatterers). The reference concentrations are called $R100$ and $P100$ and are composed as follows:

- $R100$ stands for a concentration of rhodamine molecules $\rho = 2.68 \cdot 10^{22}$ molecules/m^3,
- $P100$ stands for a concentration of polystyrene beads $\rho_s = 3.23 \cdot 10^{17}$ beads/m^3.

Figure 3.4 shows some different samples for a fixed concentration of rhodamine and different concentrations of beads.

3.4 Emission spectra

Here I will present the results obtained by shining the samples with the laser at different wavelengths. In the range of frequencies where Kennard-Stepanov law is satisfied, the emitted intensity is expected to be proportional to

$$I(\omega) \propto \frac{\mathcal{N}(\omega)}{e^{\beta(\hbar\omega-\mu)} - 1} \tag{3.5}$$

where the density of states is supposed to be that of an effective homogeneous medium given by

$$\mathcal{N}(\omega) = \frac{\omega^2 n_h^3}{\pi^2 c^3}. \tag{3.6}$$

Here n_h is the host medium refractive index. n_e is the effective one obtained by averaging over all possible realizations of the disorder. For a dilute system it is possible to assume $n_e = n_h$.

Figure 3.4: Samples from $P300R20$ to $P1R20$, where the concentration of rhodamine is fixed at $\rho = 5.36 \cdot 10^{21}$ molecules/m^3 and one of beads varies from a maximal one of $\rho_s = 9.69 \cdot 10^{17}$ beads/m^3 (left-most) to a minimal one of $\rho_s = 3.23 \cdot 10^{15}$ beads/m^3.

Therefore, by taking the logarithm of Eq. (3.5) normalized with respect to the incident power, and considering that $\beta(\hbar\omega - \mu) \gg 1$, one obtains

$$\log_{10}\left(\frac{I(\omega)}{I_0}\right) \propto \log_{10}\left(\mathcal{N}(\omega)\right) - \frac{\beta(\hbar\omega - \mu)}{\ln(10)} - \log_{10}(I_0). \tag{3.7}$$

This means that a straight line is expected to arise if the term $\log_{10}\left(\mathcal{N}(\omega)\right)$ is subtracted, if thermalization is reached and where the Kennard-Stepanov law is satisfied. Moreover, by taking the derivative of Eq. (3.7) and subtracting the term that arises from the derivative of the density of states, one expects to obtain a plateau given by

$$\frac{d}{d\omega}\log_{10}\left(\frac{I(\omega)}{I_0}\right) - \frac{\mathcal{N}'(\omega)}{\mathcal{N}(\omega)} = -\frac{\beta\hbar}{\ln(10)}. \tag{3.8}$$

We are now going to apply this rationale to the experimental data.

3.4.1 Samples with fixed density of dyes and variable density of scatterers

Now I will present the results for a fixed concentration of rhodamine, namely $R20$, and varying the concentration of beads. The following table summarizes the properties of the presented samples

Sample	R/ℓ_t	τ_D/τ_a
P300R20	26	29
P200R20	21	20
P150R20	16	14
P100R20	11	9
P50R20	5	4

Table 3.1: Samples' ratio τ_D/τ_a and R/ℓ_t

.

According to the ratio presented in Tab. 3.1 the samples that can be considered in the diffusive regime are those from $P300R20$ to $P50R20$ (i.e., $R \gg \ell_t$). Therefore, thermalization is expected

Sample	R/ℓ_s
P10R20	2
P5R20	1

Table 3.2: Samples' ratio R/ℓ_s

.

to be observed for $P300 \longrightarrow P100$ since $\tau_D/\tau_a \gg 1$, while no thermalized spectrum is expected to arise for samples with $P < 50$. The last two samples $P10$ and $P5$ are neither in the diffusive regime nor in the ballistic one since $R/\ell_s \approx 1$, see table.

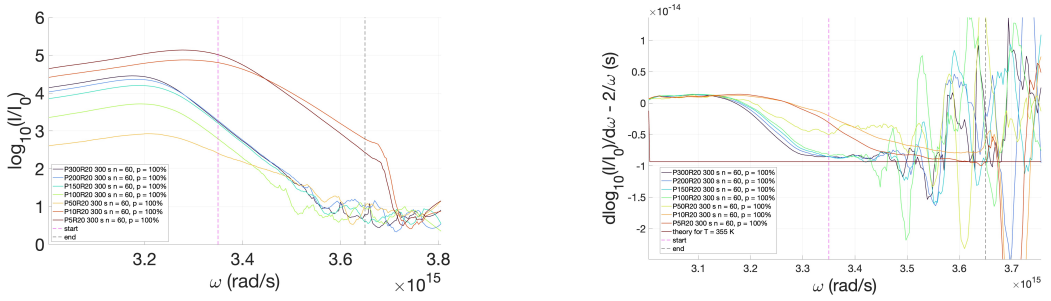

(a) Logarithm of normalized intensities.

(b) Corrected derivative of the logarithm of the normalized intensities.

Figure 3.5: Experimental results for the samples $P300R20 \longrightarrow P1R20$: background removed as the average intensity computed from 300 nm to 400 nm. The dashed vertical lines highlight the region where Kennard-Stepanov law is satisfied. $\lambda_{\text{laser}} = 480$ nm, bandwidth = 10 nm, Repetition Rate $r = 77.9$MHz. #s is the total amount of seconds of exposure. $n = \#$ is the number of acquisition used to obtain the data. $p = \#\%$ is the percentage of power of the pump laser.

This data have been obtained by shining the sample with a laser beam at 480 nm, a bandwidth of 10 nm and repetition rate of $r = 77.9$MHz. The latter value means that there is a time interval $\Delta t = 1/r = 12.5$ ns between each laser pulse. In order to improve the signal to noise ratio, the spectra have been taken in n different acquisitions and then summed together. Indeed, the signal increases proportionally to n while the noise to $\sqrt{n}$. This leads to a signal-to-noise ratio that goes like $\sqrt{n}$.

From Fig. 3.5b it is possible to see a change of behavior: at the beginning of the region where Kennard-Stepanov law is satisfied (marked by vertical dashed lines) all concentrations $P > 50$ approach a constant value close to the theoretical one obtain with Eq. (3.8) at effective temperature found in Eq. (3.2). $P10$ and $P5$ do not reach any constant value except for a small range of frequencies at end of the interest region. This could be due to an incomplete process of thermalization. The behavior obtained for $P50$ is different from the other data and is not understood yet.

To reduce the time needed to take each measurement and to increase the emitted intensity, the very same measurements have been taken with the laser at 460 nm with a bandwidth of 50 nm. This is done to take advantage of the presence of a small tail in the absorption cross section in Fig. 3.2a at higher frequencies (lower wavelengths): shining the sample on this tail would allow to have a more efficient absorption of the pump laser. This translates in a higher number of excited molecules. Also in this case, the pattern observed in the measurements taken at 480 nm is confirmed.

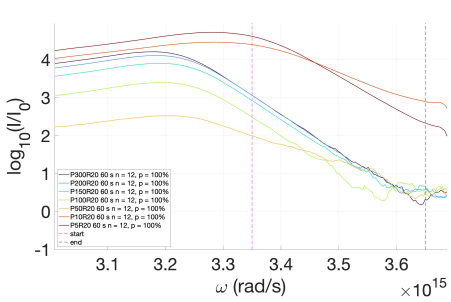

(a) Logarithm of normalized intensities.

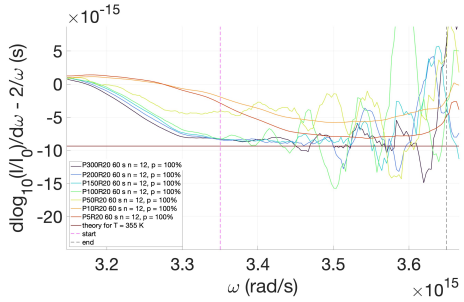

(b) Corrected derivative of the logarithm of the normalized intensities.

Figure 3.6: Experimental results for the samples $P300R20 \longrightarrow P1R20$: background removed as the average intensity computed from 300 nm to 400 nm. The dashed vertical lines highlight the region where Kennard-Stepanov law is satisfied. $\lambda_{\text{laser}} = 460$ nm, bandwidth = 50 nm, Repetition Rate $r = 77.9$MHz. #s is the total amount of seconds of exposure. $n = \#$ is the number of acquisition used to obtain the data. $p = \#\%$ is the percentage of power of the pump laser.

From the measurements taken on the sample filled with polystyrene microbeads with concentration $P > 50$, it is noticeable that a constant plateau is reached slightly before the beginning of the region where the Kennard-Stepanov law is satisfied, both in the measurements at 480 nm and 460 nm. This could be caused by a modification of the spectrum due to a preferential reabsorption of some frequencies that would shift the spectrum towards the red.

3.4.2 Samples with different densities of dyes without scatterers

Here I will present the measurements conducted on a set of samples with varying concentration of R6G but without scatterers. The absence of scatterers implies that the time that plays a role now is the ballistic one. The following table summarizes the ratio $\tau_b/\tau_a = R/v_E$ for the samples that will be shown in the following.

Sample	τ_b/τ_a
R100	15.3
R50	7.6
R40	6.1
R30	4.6
R25	3.8
R20	3.1
R10	1.5
R5	0.7
R1	0.2

Table 3.3: Samples' ratio τ_b/τ_a.

This data have been obtained by shining the sample with a laser beam at 480 nm, a bandwidth of 10 nm and repetition rate of $r = 77.9$MHz. In this case, Fig. 3.7a shows that the maximum of the emission spectra shifts towards lower energies when the concentration increases. This is due to the reabsorption of the emitted photons by the dye solution itself. In Fig. 3.7b are reported

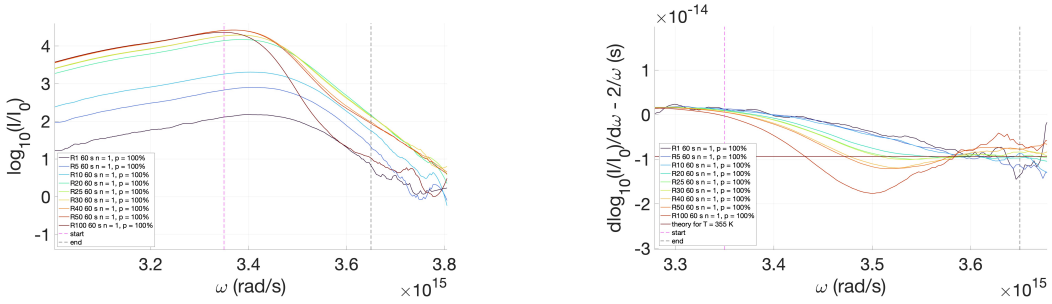

(a) Logarithm of normalized intensities.

(b) Corrected derivative of the logarithm of the normalized intensities.

Figure 3.7: Experimental results for the samples $R100 \longrightarrow R1$: background removed as the average intensity computed from 300 nm to 400 nm. The dashed vertical lines highlight the region where Kennard-Stepanov law is satisfied. $\lambda_{\text{laser}} = 480\,\text{nm}$, bandwidth $= 10\,\text{nm}$, Repetition Rate $r = 77.9\text{MHz}$. $\#\,\text{s}$ is the total amount of seconds of exposure. $n = \#$ is the number of acquisition used to obtain the data. $p = \#\%$ is the percentage of power of the pump laser.

the derivatives of the logarithm of the normalized intensity for a comparison with the previous data. The behavior is completely different with respect to the data shown in Fig. 3.6b.

3.4.3 Samples with a variable density of dyes and a fixed density of scatterers

In this section, I will present the results obtained by keeping the concentration $P200$ fixed and varying the concentration of rhodamine R from 40 to 1. The diffusive regime is valid if $R/\ell_t \gg 1$ and all the samples satisfy this requirement. In this regime, the Thouless time $\tau_H = \tau_D$ and the ratio τ_D/τ_a is reported on Tab. 3.4.

Sample	τ_D/τ_a
P200R40	81
P200R30	60
P200R25	50
P200R20	40
P200R10	20
P200R5	10
P200R1	2

Table 3.4: Samples' ratios τ_D/τ_a

The samples presented in Tab. 3.4 have been shined with a laser at 480 nm, a bandwidth of 10 nm, and a repetition rate $r = 77.9\,\text{MHz}$. The corresponding results, i.e. the logarithm of the spectrum and its corrected derivative, are reported in Fig. 3.8a and 3.8b respectively. From the curves reported in Fig. 3.8b, a change of behavior can be noticed from the highest concentration of rhodamine to the lowest ones: the theoretical value obtained with Eq. (3.8) at the effective temperature given by Eq. (3.2) is reached for the concentrations characterized by a much larger diffusive time than the absorption one for $R > 10$. It is possible to notice that the plateau is reached at lower frequencies with respect to those where Kennard-Stepanov is satisfied. As

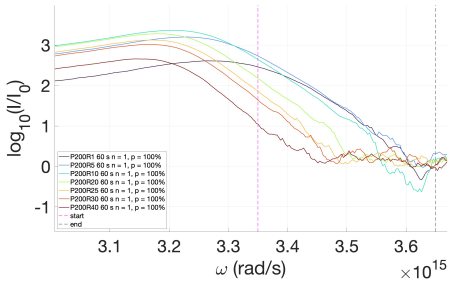

(a) Logarithm of normalized intensities.

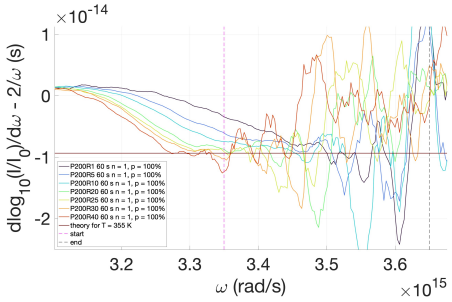

(b) Corrected derivative of the logarithm of the normalized intensities: these have been obtained by subtracting the term $\mathcal{N}'/(\omega)\mathcal{N}(\omega) = 2/\omega$ from the derivative. I will call it plateau in the next pages.

Figure 3.8: Experimental results for the samples $P200R40 \longrightarrow P200R1$: background removed as the average intensity computed from 300 nm to 400 nm. The dashed vertical lines highlight the region where Kennard-Stepanov law is satisfied. $\lambda_{\text{laser}} = 480\,\text{nm}$, bandwidth $= 10\,\text{nm}$, Repetition Rate $r = 77.9\text{MHz}$. $\#\,\text{s}$ is the total amount of seconds of exposure. $n = \#$ is the number of acquisition used to obtain the data. $p = \#\%$ is the percentage of power of the pump laser.

in Sec. 3.4.1 this could be due to a modification of the spectrum due to reabsorption at given wavelengths.

3.5 Variation of the chemical potential

Although the previous results show that there is a change of behavior between the samples that are expected to undergo thermalization and the ones that are not, still the reach of a constant value for the derivative of the logarithm is not a clear signature that the Bose-Einstein distribution with a nonzero chemical potential is achieved. In fact, a black body with a zero chemical potential would present the same behavior. A way to investigate the presence of $\mu \neq 0$ could be looking for a variation of the chemical potential between two different realizations of the experiment. Indeed, the intensity of the detected light is given by Eq. (3.5), and if one introduces a constant of proportionality A that depends on the characteristics of the sample (density of molecules and density of scatterers), Eq. (3.5) can be rewritten as

$$I(\omega) = \frac{A\mathcal{N}(\omega)}{e^{\beta(\hbar\omega-\mu)} - 1}. \tag{3.9}$$

Here A is assumed to not depend on the power of the laser. This assumption is a good approximation in the case of a Lambertian (isotropic) illumination but it is not valid in the general case. It is possible then to obtain the following expression for the variation of the chemical potential:

$$\Delta\mu = \mu_2 - \mu_1 = \frac{1}{\beta}\ln\left(\frac{I_1}{I_2}\right) \tag{3.10}$$

where I_1 is the detected intensity in realization 1, and I_2 is the detected intensity in realization 2. Because of that, in the following, I will present the results obtained for a given sample but varying the power of the laser. The power of the laser has been measured with a power meter. For 480 nm with a bandwidth of 10 nm at 100% of power, the measured power is $p = 2.7 \pm 0.1\,\text{mW}$. Then measurements have been taken at 100%, 75%, and 50%. The sample under analysis in this

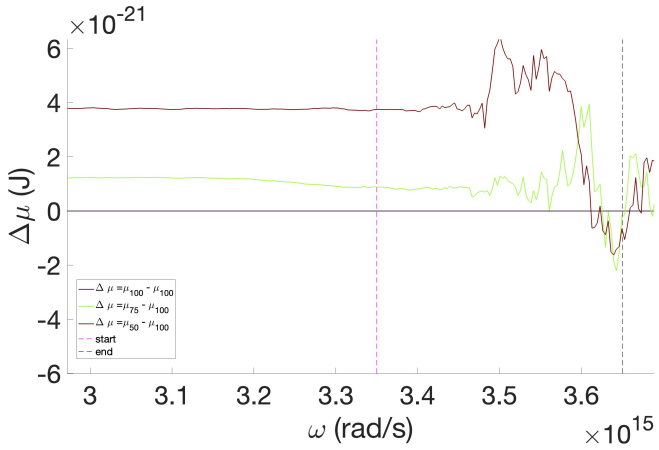

Figure 3.9: Variation the chemical potential when the power of the laser is varied.

case is $P300R20$. The reference power is 100%, which means that on the vertical axis of Fig. 3.9, it is represented

$$\Delta\mu = \mu_i - \mu_{100\%}, \tag{3.11}$$

where $i = 75\%, 50\%$. Equation (2.14) shows that the chemical potential is determined by the ratio between the excited and ground state density of the molecules, which in turn is fixed by the power of the pump laser. The latter means that decreasing the pump laser turns into a lower ratio ρ_1/ρ_0. By solving Eq. (2.14) with respect to μ, one gets

$$\mu = \hbar\omega_0 + \frac{1}{\beta}\ln\left(\frac{Z_0\rho_1}{Z_1\rho_0}\right). \tag{3.12}$$

Therefore

$$\Delta\mu = \mu_i - \mu_{100\%} = \frac{1}{\beta}\left[\ln\left(\frac{\rho_1^i}{\rho_0^i}\right) - \ln\left(\frac{\rho_1^{100\%}}{\rho_0^{100\%}}\right)\right]. \tag{3.13}$$

When $i < 100\%$, the ratio $\rho_1^i/\rho_0^i < \rho_1^{100\%}/\rho_0^{100\%}$. This means that by lowering the power of the laser, a negative $\Delta\mu$ is expected.

From Fig. 3.9, it is possible to see that the variation of the chemical potential is positive at the beginning of the region of interest and before. The large variations that appear at the middle of the region of interest are due to the fact that for those frequencies, the intensities are approaching values close to 0; therefore, a small variation of the argument of the logarithm close to 0 produces a large variation in the output. A positive variation of the chemical potential means that the assumption made in Eq. (3.9) is wrong.
This concludes this section devoted to the experimental results. In the conclusion some perspective and possible solution to the problem and inconsistencies encountered up to now will be presented.

Chapter 4

Radiative transport model with non-uniform molecules' densities

To support the previous experimental results, I have simulated the propagation of light inside the system composed of molecules and scatterers. In Sec. 2.4, the dynamic of the problem was first described by a simple diffusive model on a slab geometry to introduce the fundamental time scales that play a role in the thermalization process. As already mentioned, the considered geometry was not the one present in the experiments, but there are three other strong simplifications:

1. no external pumping was considered,
2. the density of ground state and excited molecules was supposed to be uniform in space,
3. the diffusion approximation is only valid for very large systems $R \gg \ell_t$, long time scales $t \gg R^2/D$, and weak absorption by the scatterers $\ell_a = 1/(\rho_s \sigma_{a,s}) \gg \ell_t$, where ℓ_a is the absorption mean free path of the scatterers.

To get an accurate comparison with the experiments, I will describe in the next sections a more refined model, the radiative transfer one, from which the diffusive one can be deduced by taking into account the three hypotheses of point 3 above. The two main differences are:

1. light propagation is taken into account by solving the Radiative Transfer Equation (RTE),
2. the ground states and excited molecules' densities are now allowed to vary both in space and time. In other words, we fully take into account the dynamics of the pump.

Therefore, this calls for a coupling between the RTE and a rate equation for the densities. Both of them have been implemented in a parallelized code that has been running on a cluster of processors available at Institut Langevin.

4.1 Radiative Transfer Equation

In App. A is presented a phenomenological derivation of the Radiative Transfer Equation (RTE). It is a partial differential equation that describes the evolution of the specific intensity $I(\mathbf{r}, \mathbf{u}, t, \omega)$ of the electromagnetic field. $I(\mathbf{r}, \mathbf{u}, t, \omega)$ can be seen as a local and directional radiative flux of photons at position $\mathbf{r}$, in direction $\mathbf{u}$, at time t for the frequency ω. It is linked to the number of photons per unit volume by

$$n(\mathbf{r}, t, \omega) = \frac{1}{v_E \hbar \omega} \int_{4\pi} d\mathbf{u} I(\mathbf{r}, \mathbf{u}, t, \omega). \tag{4.1}$$

Already taking into account the presence of the molecules the RTE is given by [1] ,

$$\left(\frac{1}{v_E}\frac{\partial}{\partial t} + \mathbf{u}\cdot\nabla_{\mathbf{r}}\right) I(\mathbf{r},\mathbf{u},t,\omega) = -\sigma_a(\omega)[\rho - \rho_1(\mathbf{r},t)]I(\mathbf{r},\mathbf{u},t,\omega) + \sigma_{em}(\omega)\rho_1(\mathbf{r},t)I(\mathbf{r},\mathbf{u},t,\omega) + \sigma_e(\omega)\rho_1(\mathbf{r},t)v_E\frac{\mathcal{N}(\omega)}{4\pi} - \left(\frac{1}{\ell_s(\omega)} + \frac{1}{\ell_a(\omega)}\right) I(\mathbf{r},\mathbf{u},t,\omega) + \frac{1}{\ell_s(\omega)}\int_{4\pi} d\mathbf{u}' p(\mathbf{u}\cdot\mathbf{u}',\omega) I(\mathbf{r},\mathbf{u}',t,\omega) + S(\mathbf{r},t,\omega), \tag{4.2}$$

where

- the left hand term is the transport operator applied to the specific intensity;
- the right hand side describes all the losses and gains due to, in the order they appear in the equation, absorption, stimulated and spontaneous emission by the dye molecules, extinction due to the presence of the scatterers, a gain term due to the scattering process that takes into account all the photons coming from direction $\mathbf{u}'$ and scattered in direction $\mathbf{u}$ ($p(\mathbf{u}\cdot\mathbf{u}',\omega)$ is called phase function and it represents the probability for a photon coming from direction $\mathbf{u}'$ to be scattered in direction $\mathbf{u}$, see App. A for more details) and finally a source term to model the pump laser.

Equation (4.2) is not enough to describe the dynamics of the full system. Indeed it needs to be coupled with a rate equation for the density of excited dye molecules $\rho_1(\mathbf{r},t)$ given by

$$\frac{\partial\rho_1(\mathbf{r},t)}{\partial t} = v_E[\rho - \rho_1(\mathbf{r},t)]\int_{\mathbb{R}} d\omega\sigma_a(\omega)n(\mathbf{r},t,\omega) - \rho_1(\mathbf{r},t)\int_{\mathbb{R}} d\omega\sigma_{em}(\omega)n(\mathbf{r},t,\omega) - \rho_1(\mathbf{r},t)\int_{\mathbb{R}} d\omega\sigma_{em}(\omega)\mathcal{N}(\omega). \tag{4.3}$$

On the right hand side of this last equation, in the order they appear, are taken into account all the process that lead $\rho_1(\mathbf{r},t)$ to change: absorption, stimulated and spontaneous emission. The coupling of Eq. (4.2) and Eq. (4.3) gives a full description of the dynamics of the problem.

4.2 Numerical algorithm

In this section, I will describe the numerical algorithm and its implementation on the processor cluster available at Institut Langevin. Equation (4.2) and Eq. (4.3) can be numerically solved with the Monte Carlo method. An iterative process is necessary because of the coupling. Space, time, frequency, and the angles are discretized. The algorithm follows the following scheme:

1. The number density of excited molecules is initialized to $\rho_1(\mathbf{r},0) = 0$.
2. Equation (4.2) is solved with a Monte Carlo [13] method for every frequency with the fixed density of excited molecules $\rho_1(\mathbf{r},t)$. This consists in sending, for each frequency, a given number of energy packets (Monte Carlo trials) inside the system and making them perform a random walk where the direction of each step is generated from the probability given by the phase function $p(\mathbf{u}\cdot\mathbf{u}',\omega)$ and its length s from $p(s) = e^{-s/\ell_s(\omega)}/\ell_s(\omega)$. It is important to remark that this is just a stochastic method that converges to the solution of the equation, it does not capture the real physical mechanism of scattering.
3. This step provides a map of the density of photons $n(\mathbf{r},t,\omega)$.
4. Using the previous map for $n(\mathbf{r},t,\omega)$, Eq. (4.3) is solved using the finite difference method. This yields a map of the density of excited molecules $\rho_1(\mathbf{r},t)$.

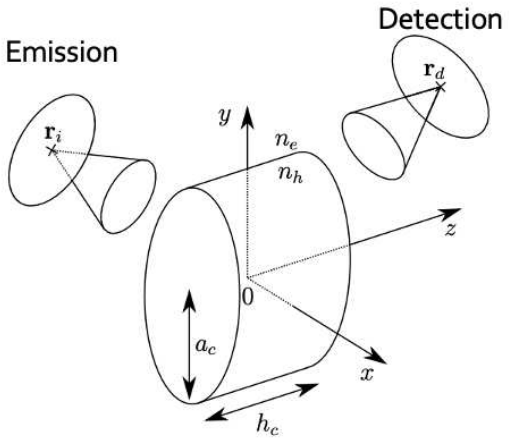

Figure 4.1: Geometry of the system under analysis with the geometrical parameter definitions

5. Iterate starting from step 2 with $\rho_1(\mathbf{r}, t)$ found at step 4

The code that implements this algorithm is written in Fortran 90 and is parallelized in a hybrid version using OpenMP/MPI.

Figure 4.1 shows the geometry of the problem that mimics the experiment. The molecules and the scatterers are considered to be inside a water solution in a cylinder of height h_c and radius a_c. n_h is the refractive index of water and n_e is the external refractive index. The source term is represented by the pump laser and is modeled as a Gaussian beam of waist w_i, centered at position $\mathbf{r}_i$, along direction $\mathbf{u}_i$ on a solid angle defined by the numerical aperture $\mathrm{NA}_i = \sin(\theta_i)$ (the illumination is considered to be uniform over this angle range). The laser pulses are considered as Gaussian pulses of width t_i and total energy E_i.

4.3 Input parameters

Here I will describe the input parameters needed to perform the simulations. A crucial parameter that was given as input to the simulations is the number of Monte Carlo trials. This was chosen by running the simulation for higher and higher numbers of trials until reaching convergence. The other parameters can be grouped into two categories: discretization parameters and physical ones. The first were chosen to be sensitive to all the physical quantities that play a role in the scattering and thermalization process, while the latter were tuned to match the experimental realization.

The discretization is needed to implement the Monte Carlo algorithm for Eq. (4.2) and the finite difference method used for Eq. (2.26). Therefore,

- the spatial discretization of the cylindrical cell was chosen to obtain space steps smaller than the smallest scattering mean free path $\ell_s(\omega) = 1/(\rho_s \sigma_s(\omega))$;
- time discretization was chosen to obtain smaller time steps than the smallest time that plays a role in all the dynamics, which is $\tau_a'(\omega) = 1/(v_E \sigma_a'(\omega))$ in the thermalized regime;

- frequency discretization was chosen to have enough points in the region where the Bose-Einstein distribution is expected to be achieved, namely where Kennard-Stepanov law is satisfied;
- angles discretization for the computation of the phase function was chosen to take into account correctly all directions.

The physical ones were:

- the radius and the height of the cylindrical cell;
- the frequency range that was chosen to incorporate the full molecular dynamics, therefore much broader than the frequency range where Kennard-Stepanov law is satisfied, namely from $2.5 \cdot 10^{15}$ rad/s to $4.5 \cdot 10^{15}$rad/s;
- the initial and final times and the number of laser pulses; these were chosen taking into account that in the simulations the pulses are modeled as Gaussian functions in time with a temporal standard deviation of $\sigma_t = 100\,\text{ps}$ and the time interval between two pulses is given by $\Delta t = 1/r = 12.5\,\text{ns}$ where $r = 77.9\,\text{MHz}$ is the repetition rate of the laser available at Institut Langevin for this experiment. Therefore these parameters were tuned to have at least 2 pulses between the initial and final times to avoid to overcome the transient phase and to keep the time needed to run the simulation within reasonable order of magnitude;
- the density of scatterers and the density of molecules were chosen to match those studied in the experiments;
- the illumination parameters such as: incident position, beam waist of the beam, incident direction, numerical aperture of illumination, energy per pulse, time interval between the pulses, duration of each pulse, and frequency of the laser were all chosen to be the same as the performed measurements;
- the detection parameters can be chosen to detect all the photons emitted over $4\pi\,\text{sr}$ or to detect the photons emitted in a certain direction. In the latter case, the position, radius, direction, and numerical aperture of detection need to be specified. Even though in the experiments the detection was always directional, in the simulations the detection was always performed over all directions. This is because first the output flux can be considered isotropic, except for the laser frequency, thanks to spontaneous emission and scattering. Secondly a directional detection needs a higher number of Monte Carlo trials that turns into a longer computing time.

4.4 Numerical results

Here I will present the results obtained from the simulations that I have been running. The parallelization allowed to run a simulation simultaneously on 500 CPUs. Though the amount of time needed to complete one is of the order of several days ($\approx 5 - 10$ days). The simulations output is the detected flux as a function of time and frequency . This is formally given by

$$\phi(\omega, t) = \int_{\Sigma} \left[\int_{4\pi} I(\mathbf{r}, \mathbf{u}, t, \omega) \mathbf{u} d\mathbf{u} \right] \cdot \mathbf{n} dS \tag{4.4}$$

where the last surface integral is performed on the surface Σ of the detector. In the post-processing analysis, an integration of $\phi(\omega, t)$ in time over the last cycle is performed in order to avoid the transient regime. This allows to obtain the intensity $I(\omega)$ as a function of frequency only. Then,

the same analysis applied to the experimental data has been applied to the simulated $I(\omega)$. I will present the first simulation that gave results comparable to those obtained in the experiments. This was done for $P300R20$ because this combination of concentration is expected to undergo thermalization. The input pulses were chosen to have a central wavelength of 480 nm as in the experiments. From the measurement of the power $pow = (2.7 \pm 0.1)$ mW of the laser at 480 nm with 100% power and given the repetition rate $r = 77.9$MHz, it was possible to derive the energy per pulse E in these conditions:

$$E = \frac{pow}{r} = 3.47 \cdot 10^{-11}\text{J}. \tag{4.5}$$

This value was set as a reference, therefore in the following all percentages of power p refer to this value as 100%.

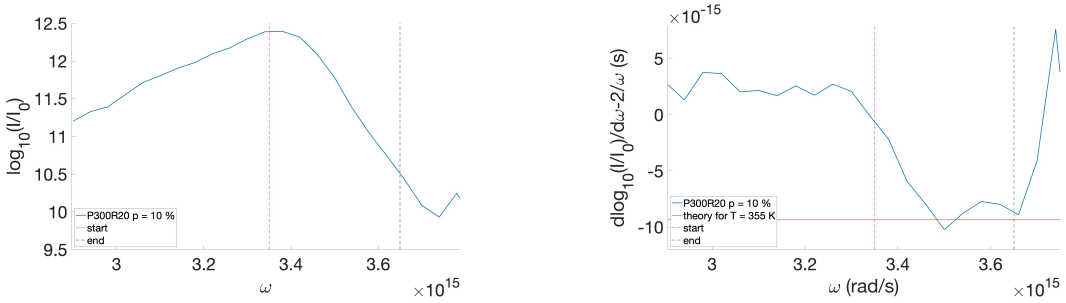

(a) (b)

Figure 4.2: Simulated results for the concentration $P300R20$. The dashed vertical lines highlight the region where Kennard-Stepanov law is satisfied. $p = \#\%$ is the percentage of power of the laser pulses with respect to the reference. (a) Logarithm of normalized intensities. (b) Corrected derivative of the logarithm of the normalized intensities.

Figure 4.2 show that both in the logarithm of the normalized intensity and in the corrected derivative of it the Bose-Einstein behavior seems to be achieved, but the number of points in the frequency window of interest was still not enough. In order to improve the result, the frequency discretization step size should be reduced, but this would require more computation time. This was done for a fewer concentration of scatterers in order to limit the increase of the computation time.

The results are plotted in Fig. 4.3 for the last four concentrations reported in Tab. 3.4. At the moment, it is not possible to simulate concentrations of rhodamine that exceed $R20$ because increasing this concentration results in lower and lower values of τ_a', leading to finer and finer discretization of the time interval. Such a fine discretization would require an amount of memory not available in the cluster of Institut Langevin. Despite this, it is possible to compare these results with the same concentrations shown in Fig. 3.8b.

This is done in Fig. 4.4 that shows the data obtained from the experiments and those obtained from the simulations on the same graph. It is possible to see that, except for a redshift of the experimental data with respect to the simulated ones, the pattern observed is the same in both the simulations and experiments. By comparing the experimental results given in Fig. 3.8 and Fig. 3.7 it is possible to notice that one of the effect of the presence of the scatterers is a redshift of the curves relative to the sample with scatterers with respect to those without. This can be seen clearly by comparing the starting point of the drop of the corrected derivative of the logarithm of the normalized intensity: in Fig. 3.8b (samples with scatterers) all the derivatives start to decrease before the point where they start to decrease in Fig. 3.7b (samples without scatterers).

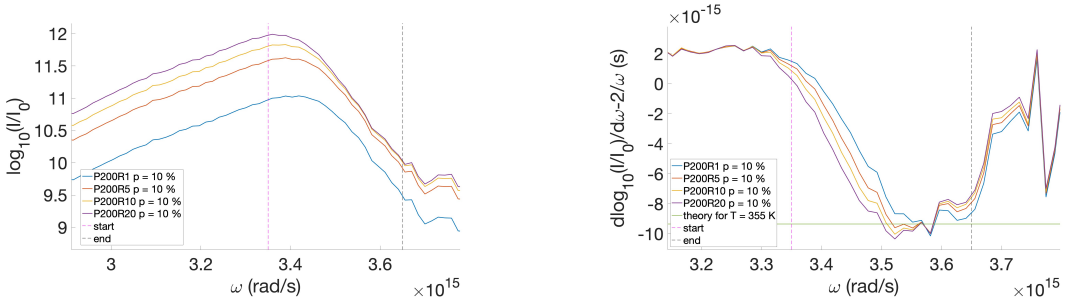

(a) (b)

Figure 4.3: Simulated results for the concentration $P200R20 \longrightarrow P200R1$. The dashed vertical lines highlight the region where Kennard-Stepanov law is satisfied. $p = \#\%$ is the percentage of power of the laser pulses with respect to the reference. (a) Logarithm of normalized intensities. (b) Corrected derivative of the logarithm of the normalized intensities.

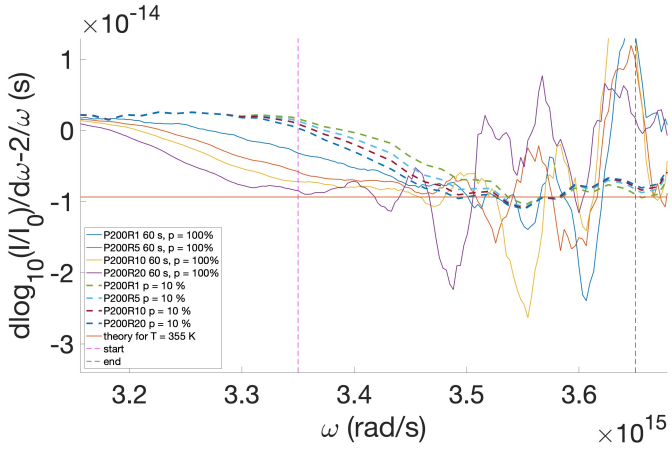

Figure 4.4: Comparison of experimental and simulated data for $P200R20 \longrightarrow P200R1$. The solid lines represent the experimental data while the dashed lines represent the simulated ones. The dashed vertical lines highlight the region where Kennard-Stepanov law is satisfied. $p = \#\%$ is the percentage of power of the laser pulses with respect to the reference.

This suggest that the simulation is not able to capture the presence of the scatterers. In order to investigate this problem the simulations were run for a fixed concentration of rhodamine, namely $R20$, and for three different concentrations of beads $P150$, $P100$, $P50$.

The results are shown in Fig. 4.5. Clearly, in this case, the simulation fails to discriminate the different concentrations of beads. In order to check if this problem persists in two extreme situations, it is possible to compare the output of the simulations for a set of input parameters where the concentration of beads approaches 0 and one with a high concentration of beads, namely $P200$, for a fixed concentration of rhodamine, $R20$.

From Fig. 4.6 it is now evident that the current algorithm is not sensitive enough to the concentration of scatterers. Indeed, the redshift of the curve relative to $P200R10$ with respect to $R10$ is significantly larger in the experimental data than in the simulated ones.
As a conclusion of this chapter it is possible to notice that the main problem encountered in the

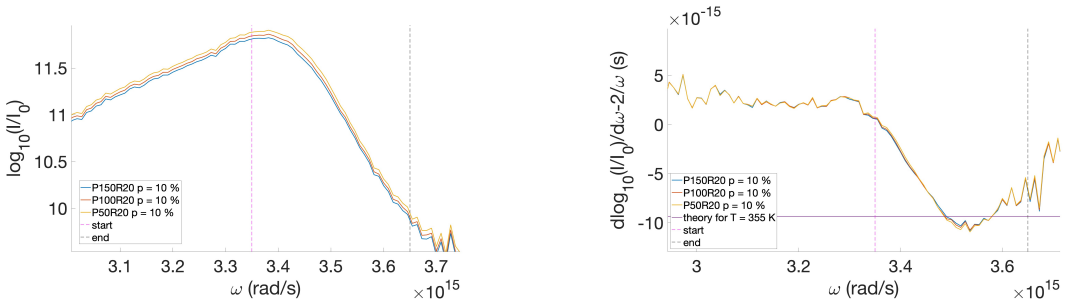

Figure 4.5: Simulated results for the concentrations $P150R20 \longrightarrow P50R20$. The dashed vertical lines highlight the region where Kennard-Stepanov law is satisfied. $p = \#\%$ is the percentage of power of the laser pulses with respect to the reference. (a) Logarithm of normalized intensities. (b) Corrected derivative of the logarithm of the normalized intensities.

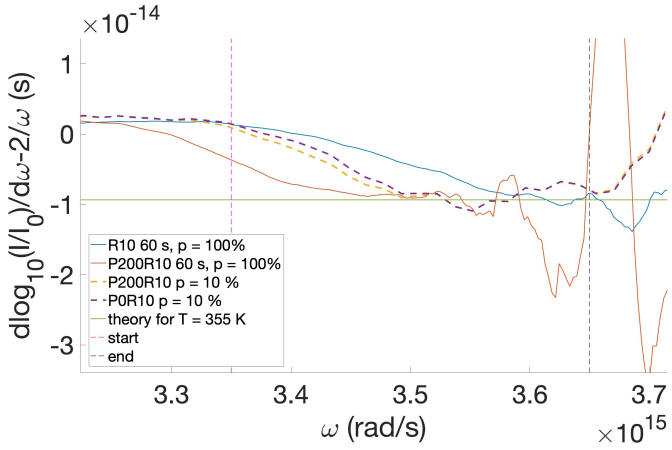

Figure 4.6: Comparison between extreme situations for both experimental and simulated data. The solid lines represent the experimental data while the dashed lines represent the simulated ones. The concentrations shown are $P200R10$ and $R10$. The dashed vertical lines highlight the region where Kennard-Stepanov law is satisfied. $p = \#\%$ is the percentage of power of the laser pulses with respect to the reference.

simulations is the effect of the scatterers that do not reproduce the same results obtained in the experiments. In the conclusion I will explain a possible way to investigate this problem.

Chapter 5

Conclusions

As a conclusion of this work, it is possible to say that the experimental data seem to show that we are moving in the right direction. There is a clear change in behavior between the spectra that are expected to be thermalized and those that are not. However, the fact that the corrected derivatives of the logarithm of the normalized intensities reach a plateau at the effective temperature obtained by the linear fit of the Kennard-Stepanov law is still not a clear indication that the gas of photons under analysis has a non-vanishing chemical potential. Indeed, the same behavior would be observed if $\mu = 0$. This calls for a change of paradigm in the data analysis to find a clear proof that μ is non-vanishing. This was the spirit of the last analysis that I have done and presented in Sec. 3.5. However, this calculation brings to a non-physical result, that is that the number of excited molecules decreases as the pump power increases. There can be two reasons for that. The first one is that the hypothesis that lead to Eq. (3.9) are not well-adapted to our system. As explained in Sec. 3.5, the calculation supposes a lambertian source, which is not the case in our measurements. The second one could be photobleaching of the molecules during the acquisition. If a dye molecule undergoes too many cycles of absorption and emission, there is a probability it will fall into a dark state which is not the fundamental one, without the possibility of returning to it. Because of that, no more absorption events are allowed for that molecule. This process could change the effective concentration of molecules in the samples i.e. the number of molecules in the ground state that can be excited, making a certain realization of the experiment not repeatable. This aspect, along with obtaining a clear signature of thermalization, will be the starting point of my PhD. A way to measure a non-vanishing chemical potential could be to exploit an integrating sphere to collect all the photons emitted by the sample. This could be a way to estimate the number of photons that are trapped in the solution and therefore the chemical potential.

Moreover, several improvements need to be made on the numerical side as well. The code that I have been using up to now is still a preliminary version. It must be optimized to obtain faster results. Also, as mentioned at the end of Sec. 4.4, the current algorithm is not sufficiently sensitive to variations in the concentration of scatterers. We believe that the problem is a convergence issue. This aspect will be investigated by running the simulations in a simpler slab geometry with a simpler version of the code (steady state one), where it could be easier to understand the problem.

Finally, the direction of this work will move towards Bose-Einstein condensation (BEC) of photons in disordered scattering media. This corresponds to a macroscopical occupation of the ground state of the gas of photons. This will be achieved by investigating new fluorophores such as quantum dots and nano-platelets because of their interesting absorption and emission properties, and new scatterers such as titanium dioxide. More importantly, the main idea to achieve a BEC of photons is to exploit photonic glasses as scattering media. The main difference

between a photonic glass and the scatterers that have been used up to now is that in the former, the disorder correlations allow to have a more well-defined spectral density of modes. Indeed a photonic glass is static semi-disordered material. This could allow us to choose which modes will be populated and, eventually, the fundamental one.

Appendix A

Phenomenological derivation of the Radiative Transfer Equation (RTE)

The RTE describes the temporal and spatial evolution of the specific intensity $I(\mathbf{r}, \mathbf{u}, t, \omega)$, defined as the spatio-temporal Fourier transform of the correlation of the electric field. It can be rigorously deduced from Maxwell's equations, but here I will present an easier phenomenological approach. This corresponds to an energy balance. Let's first introduce

$$P(\mathbf{r}, \mathbf{u}, t, \omega) = I(\mathbf{r}, \mathbf{u}, t, \omega)\, \mathbf{u} \cdot \mathbf{n}\, dS\, d\mathbf{u}\, d\omega. \tag{A.1}$$

It is possible to prove that P is the power passing through a surface dS centered at position $\mathbf{r}$ in a solid angle $d\mathbf{u}$ centered along direction $\mathbf{u}$ in the frequency window $[\omega, \omega + d\omega]$ at time t, where $\mathbf{n}$ is a unit vector perpendicular to the surface dS. Fig. A.1 shows the notations previously defined. Let's consider an elementary volume dV as in Fig. A.2 containing both the fluorescent molecules and the scattering medium.

The latter is considered to be averaged over all its possible realizations in order to account for its effect using an absorption coefficient $1/\ell_a$ and a scattering coefficient $1/\ell_s$. Both of these

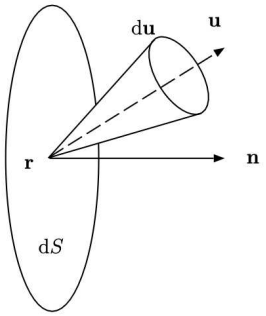

Figure A.1: Representation of the infinitesimal surface used to define P

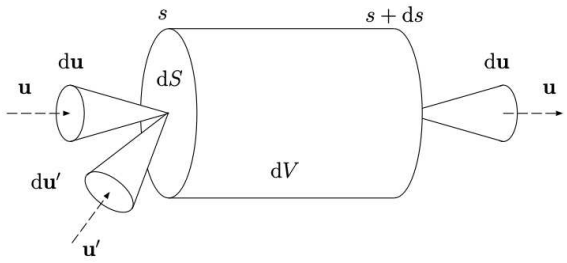

Figure A.2: Representation of the infinitesimal volume dV.

naturally appear in more rigorous theory. The absorbed power in dV is given by

$$dP_a(\mathbf{r},\mathbf{u},t,\omega) = -\frac{1}{\ell_a(\omega)} I(\mathbf{r},\mathbf{u},t,\omega)ds - \sigma_a(\omega)\rho_0(\mathbf{r},t)I(\mathbf{r},\mathbf{u},t,\omega)ds, \tag{A.2}$$

where the first term on the right-hand side describes the absorption by the scatterers and the second term describes the absorption by the molecules. Equivalently, the scattered power leads to

$$dP_s(\mathbf{r},\mathbf{u},t,\omega) = -\frac{1}{\ell_s(\omega)} I(\mathbf{r},\mathbf{u},t,\omega)dS. \tag{A.3}$$

ℓ_s and ℓ_a appearing in the last two equations are defined by

1. $\ell_s(\omega) = 1/\rho_{scatt}\sigma_s(\omega)$ is the scattering mean free path. Here, ρ_{scatt} is the number of scatterers per unit volume and $\sigma_s(\omega)$ is the scattering cross-section. ℓ_s can be seen as the average distance traveled by a photon between two scattering events.

2. $\ell_a(\omega) = 1/\rho_{scatt}\sigma_a^{scatt}(\omega)$ is the absorption mean free path. Here, $\sigma_a^{scatt}(\omega)$ is the absorption cross-section of the scatterers. This length can be seen as the distance after which, on average, a photon is absorbed.

Equation (A.2) and Eq. (A.3) give rise to the lost power

$$\begin{aligned} dP_l(\mathbf{r},\mathbf{u},t,\omega) &= -\left[\frac{1}{\ell_a(\omega)} + \frac{1}{\ell_s(\omega)}\right] I(\mathbf{r},\mathbf{u},t,\omega)ds - \sigma_a(\omega)\rho_0(\mathbf{r},t)I(\mathbf{r},\mathbf{u},t,\omega)ds = \\ &= -\frac{1}{\ell_e(\omega)} I(\mathbf{r},\mathbf{u},t,\omega)ds - \sigma_a(\omega)\rho_0(\mathbf{r},t)I(\mathbf{r},\mathbf{u},t,\omega)ds. \end{aligned} \tag{A.4}$$

Here I have defined

$$\frac{1}{\ell_a(\omega)} + \frac{1}{\ell_s(\omega)} = \frac{1}{\ell_e(\omega)} \tag{A.5}$$

as the extinction coefficient. A gain term arises from the power scattered from direction $\mathbf{u}'$ to direction $\mathbf{u}$ (first term), stimulated emission (second term), spontaneous emission (third term) by the molecules, and the pump laser (fourth term):

$$\begin{aligned} dP_g(\mathbf{r},\mathbf{u},t,\omega) = \frac{1}{\ell_s(\omega)} \int_{4\pi} d\mathbf{u}' p(\mathbf{u}\cdot\mathbf{u}',\omega) I(\mathbf{r},\mathbf{u},t,\omega)ds + \\ +\sigma_{em}(\omega)\rho_1(\mathbf{r},t)I(\mathbf{r},\mathbf{u},t,\omega)ds + \sigma_e(\omega)\rho_1(\mathbf{r},t)v_E\frac{\mathcal{N}(\omega)}{4\pi}ds + S(\mathbf{r},t,\omega)ds. \end{aligned} \tag{A.6}$$

Here $p(\mathbf{u}\cdot\mathbf{u}',\omega)$ is called the phase function, and it is the probability for a photon coming from direction $\mathbf{u}'$ to be scattered in direction $\mathbf{u}$. The integration over the whole solid angle is needed to take into account all directions.

The energy balance implies:

$$P(\mathbf{r}+dS\mathbf{u},\mathbf{u},t+dt,\omega)-P(\mathbf{r},\mathbf{u},t,\omega)=dP_l(\mathbf{r},\mathbf{u},t,\omega)+dP_g(\mathbf{r},\mathbf{u},t,\omega). \tag{A.7}$$

Exploiting the definition of the power Def. (A.1), $\rho_0=\rho-\rho_1$, $dS=v_E dt$ and

$$\frac{1}{v_E}\frac{d}{dt}=\frac{1}{v_E}\frac{\partial}{\partial t}+\mathbf{u}\cdot\nabla_r \tag{A.8}$$

Equation (A.7) leads to the RTE:

$$\begin{aligned}\left(\frac{1}{v_E}\frac{\partial}{\partial t}+\mathbf{u}\cdot\nabla_r\right)I(\mathbf{r},\mathbf{u},t,\omega)=-\sigma_a(\omega)[\rho-\rho_1(\mathbf{r},t)]I(\mathbf{r},\mathbf{u},t,\omega)+\\ \sigma_{em}(\omega)\rho_1(\mathbf{r},t)I(\mathbf{r},\mathbf{u},t,\omega)+\sigma_e(\omega)\rho_1(\mathbf{r},t)v_E\frac{\mathcal{N}(\omega)}{4\pi}-\mu_e(\omega)I(\mathbf{r},\mathbf{u},t,\omega)+\\ \frac{\mu_s(\omega)}{4\pi}\int_{4\pi}d\mathbf{u}'p(\mathbf{u}\cdot\mathbf{u}',\omega)I(\mathbf{r},\mathbf{u}',t,\omega)+S(\mathbf{r},t,\omega).\end{aligned} \tag{A.9}$$

This last equation alone is not enough to describe the full problem because, as stated before, the molecules' densities now depend on both position and time. Therefore, Eq. (4.2) has to be solved coupled with an equation that describes the rate of change for the excited molecules' densities. This is given by:

$$\begin{aligned}\frac{\partial\rho_1(\mathbf{r},t)}{\partial t}=v_E[\rho-\rho_1(\mathbf{r},t)]\int_{\mathbb{R}}d\omega\sigma_a(\omega)n(\mathbf{r},t,\omega)-\rho_1(\mathbf{r},t)\int_{\mathbb{R}}d\omega\sigma_{em}(\omega)n(\mathbf{r},t,\omega)\\ -\rho_1(\mathbf{r},t)\int_{\mathbb{R}}d\omega\sigma_{em}(\omega)\mathcal{N}(\omega).\end{aligned} \tag{A.10}$$

The number of photons per unit volume is related to the intensity by:

$$n(\mathbf{r},t,\omega)=\frac{1}{\hbar\omega v_E}\int_{4\pi}d\mathbf{u}I(\mathbf{r},\mathbf{u},t,\omega). \tag{A.11}$$

Bibliography

[1] Radiative transfer. by s. chandrasekhar. london (oxford university press) 1950. 8vo. pp. 393, 35 figures. 35s. Quarterly Journal of the Royal Meteorological Society, 76(330):498–498, 1950.

[2] Hui Cao. Random lasers: Development, features and applications. Opt. Photon. News, 16(1):24–29, Jan 2005.

[3] D. Haar. The Old Quantum Theory. Commonwealth and international library: Selected readings in physics. 1967.

[4] E. H. Kennard. On the thermodynamics of fluorescence. Phys. Rev., 11:29–38, Jan 1918.

[5] E. H. Kennard. The excitation of fluorescence in fluorescein. Phys. Rev., 29:466–477, Mar 1927.

[6] Jan Klaers, Julian Schmitt, Tobias Damm, Frank Vewinger, and Martin Weitz. Statistical physics of bose-einstein-condensed light in a dye microcavity. Phys. Rev. Lett., 108:160403, Apr 2012.

[7] Jan Klaers, Julian Schmitt, Frank Vewinger, and Martin Weitz. Bose–einstein condensation of photons in an optical microcavity. Nature, 468(7323):545–548, Nov 2010.

[8] Jan Klaers and Martin Weitz. Bose-einstein condensation of photons, 2012.

[9] D. P. Landau and K. Binder. A guide to Monte-Carlo simulations in statistical physics. Cambridge Univerity Press, 2000.

[10] V. S. Letokhov. Generation of Light by a Scattering Medium with Negative Resonance Absorption. Soviet Journal of Experimental and Theoretical Physics, 26:835, April 1968.

[11] D. E. McCumber. Einstein relations connecting broadband emission and absorption spectra. Phys. Rev., 136:A954–A957, Nov 1964.

[12] Nicholas Metropolis, Arianna W. Rosenbluth, Marshall N. Rosenbluth, Augusta H. Teller, and Edward Teller. Equation of State Calculations by Fast Computing Machines. The Journal of Chemical Physics, 21(6):1087–1092, 06 1953.

[13] Ulrich M. Noebauer and Stuart A. Sim. Monte carlo radiative transfer. Living Reviews in Computational Astrophysics, 5(1):1, Jun 2019.

[14] Max Planck. Entropie und temperatur strahlender warme. Annalen der Physik, 1:719 – 737, 1900.

[15] Max Planck. Uber das gesetz der energieverteilung im normalspectrum. Annalen der Physik, 4:553 – 563, 1900.

[16] Max Planck. Uber eine verbesserung der wienschen spektralgleichung. Verhandlungen der Deutschen Physikalischen Gesellschaft, 2:202 – 204, 1900.

[17] Max Planck. Uber irreversible strahlungsvorgange. Annalen der Physik, 1:69 – 122, 1900.

[18] Max Planck. Zur theorie des gesetzes der energieverteilung im normalspektrum. Verhandlungen der Deutschen Physikalischen Gesellschaft, 2:237 – 245, 1900.

[19] Robert T. Ross. Some Thermodynamics of Photochemical Systems. The Journal of Chemical Physics, 46(12):4590–4593, 06 1967.

[20] Julian Schmitt, Tobias Damm, David Dung, Frank Vewinger, Jan Klaers, and Martin Weitz. Thermalization kinetics of light: From laser dynamics to equilibrium condensation of photons. Phys. Rev. A, 92:011602, Jul 2015.

[21] B.I. Stepanov. Universal relation between the absorption spectra and luminescence spectra of complex molecules. Doklady Akademii Nauk SSSR, 112:839, 1957.